Fabrication of Hierarchically Porous Materials and Nanowires through Coffee Ring Effect

Sachin Khapli,[†] Ina Rianasari,[†] Thomas Blanton,[‡] James Weston,[†] Rachael Gilardetti,[§] Rodrigo Neiva,[∥] Nick Tovar,[§] Paulo G. Coelho,[†,§] and Ramesh Jagannathan*[,†]

[†]Engineering Division, New York University Abu Dhabi, Abu Dhabi, United Arab Emirates
[‡]International Centre for Diffraction Data, Newtown Square, Pennsylvania, United States
[§]Department of Biomaterials and Biomimetics, New York University College of Dentistry, New York, New York, United States
[∥]Department of Periodontology, University of Florida College of Dentistry, Gainesville, Florida, United States

Ⓢ Supporting Information

ABSTRACT: We report a versatile method for the fabrication of nanowires and hierarchical porous materials from a wide variety of ceramic materials such as $CaCO_3$, ZnO, CuO, Co_3O_4, Co-doped ZnO, and Ag_2O. The method consists of evaporation of CO_2-enriched water microdroplets (diameter ~3 μm) deposited from an aerosol onto heated substrates (T = 120 °C). A variety of porous scaffolds with 1−3 μm sized pores can be generated by tuning the process conditions. Subsequent sintering of the scaffolds is shown to generate nanosized pores in the walls of the porous scaffold creating a dual hierarchy of pore

sizes (~50 nm and 1−3 μm). We propose a mechanism for the formation of scaffolds based on the coffee-ring effect during the evaporation of microdroplets. Ostwald-ripening of $CaCO_3$ scaffolds prepared without sintering yields scaffold structures consisting of two-dimensional crystals of $CaCO_3$ that are one unit cell thick. The favorable application of $CaCO_3$ scaffolds for the enhancement of bone healing around titanium implants with improved biocompatibility is also demonstrated.

KEYWORDS: bioactive ceramics, hierarchical porous materials, calcium carbonate, two-dimensional crystals, coffee-ring effect
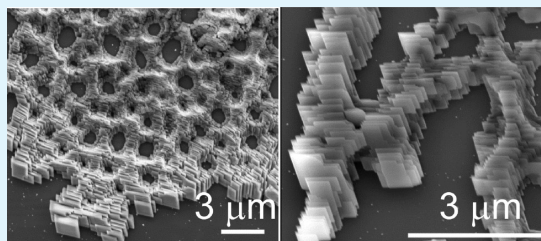
■ INTRODUCTION

Porous materials with structural hierarchy are abundant in nature, for example, diatom skeletons, corals, wood, and bone. The overall organization of mater on the macro, micro, and nanoscales in these materials results in exceptional functional properties.[1] Inspired by these natural materials, there has been considerable research on the development of hierarchically structured porous materials with numerous applications across a broad range of technologies[2] such as separation and purification of gases and liquids,[3,4] catalysis,[5] sensors,[6−9] solar cells,[10,11] fuel cells,[12] supercapacitors,[13,14] electrodes with improved properties,[15−18] and biocompatible scaffolds for promoting cell adhesion.[19−22] Most common techniques for the fabrication of such biomimetic materials utilize sacrificial templates such as colloidal crystals, emulsions, ice crystals, and gas bubbles.[2] Bottom-up approaches based on self-assembly have also been applied for fabrication of hierarchically porous materials.[23−25] Scalability of these processes as well as control over the pore size are key challenges and continue to be the topics of ongoing research.

We report a novel method for the fabrication of hierarchically porous materials through the phenomenon of coffee-ring effect, i.e., the formation of ringlike patterns during the evaporation of liquid droplets.[26] Because of the pinning of the three phase contact line during initial stages of evaporation, there is a substantial material deposition at the boundary of the

evaporating droplet, which leads to the formation of circular patterns after drying under suitable conditions. The phenomena of coffee ring effect is, however, not strictly ubiquitous, and various other patterns such as uniform and pillar-shaped deposits are also observed depending on experimental parameter variation such as solution concentration, environmental conditions, and thermal properties of the substrate.[27,28] The formation of various geometric patterns during evaporation of sessile droplets has been intensely studied and successfully utilized for the deposition of colloidal particles using macroscopic droplets of millimeter-size diameters.[28,29] However, its extension to the evaporation of microdroplets from a dense aerosol and the resulting pattern formation has been relatively unexplored so far. Here we show that, the pattern formation during evaporation of microdroplets can be utilized for the formation of porous films. In contrast, most of the conventional spray coating methods are developed to obtain continuous films.[30−32]

We utilize a supercritical CO_2 (sc-CO_2)-based nebulization process, invented by Sievers et al.,[33−37] to create dense aerosols with droplet size less than 3 μm. Along with the small size of droplets produced, this method offers the added benefit that
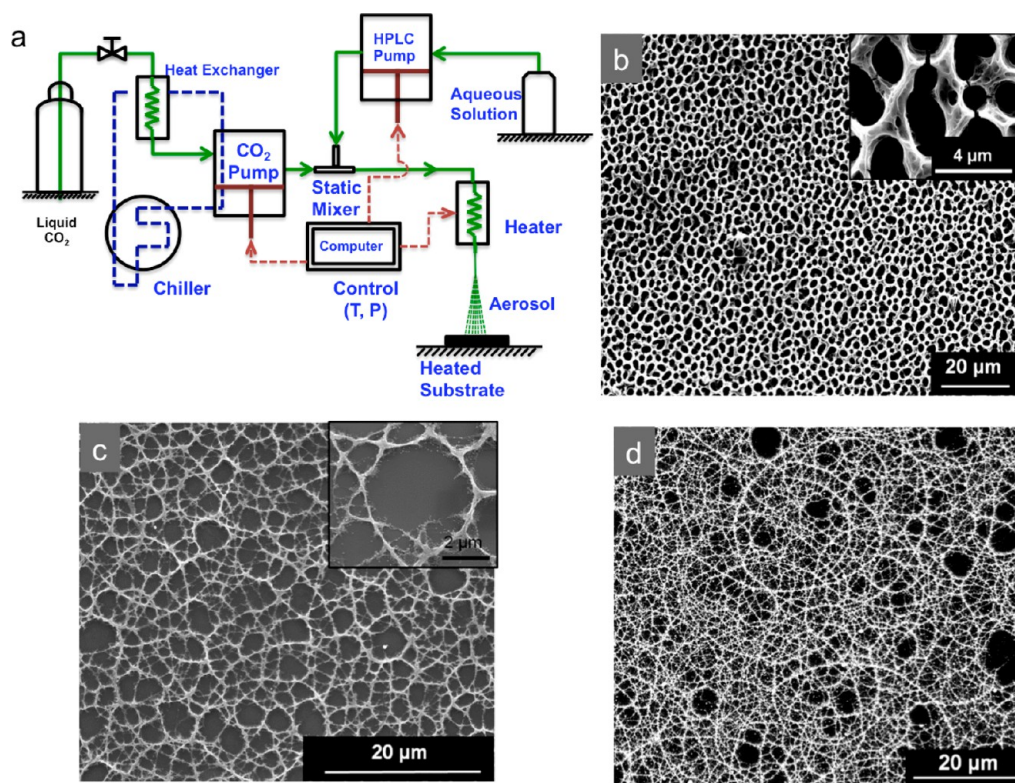
Figure 1. (a) Schematic of the process for creating micrometer-sized water droplets using sc-CO_2 and their deposition on heated substrates. (b–d) Morphologies of porous scaffolds obtained by aerosol deposition process for various materials, (b) cobalt doped zinc oxide, (c) copper oxide, and (d) silver oxide.

the aerosol droplets are saturated with carbon dioxide which is advantageous for producing porous microstructures due to the effervescence of gas bubbles during evaporation. We utilize this process for the generation of micron sized water droplets containing dissolved salts for deposition. Porous films are deposited by continuous evaporation of these microdroplets on superheated substrates at atmospheric pressure. Our method does not use any sacrificial templates to create three-dimensional scaffolds of ceramics and is applicable to a wide variety of materials such as $CaCO_3$, ZnO, CuO, Co_3O_4, Co-doped ZnO, and Ag_2O. We also report that we are able to create scaffold structures consisting of 2-dimensional crystals of $CaCO_3$ that are nominally one c-axis unit-cell length in thickness. The process is scalable and environmentally friendly because it uses sc-CO_2 as a medium for the synthesis. Finally, we demonstrate the successful application of $CaCO_3$ as a bioactive ceramic deposition for the enhancement of bone healing around titanium implants in a relevant preclinical animal model.

■ EXPERIMENTAL SECTION

Materials. Precursor materials, calcium acetate hydrate, zinc acetate, cobalt acetate, silver acetate, and copper acetate were purchased highest purity grade (99.99%) from Sigma-Aldrich. Polished silicon (100 orientation), fused quartz, and single-crystal sapphire substrates were purchased from Goodfellow Corp., USA. The substrates were cleaned by sonication in Millipore water and isopropanol followed by drying with air jet. The cleaned substrates were found to be highly hydrophilic (water contact angle below 20°). CO_2 liquid was purchased from Air Products Middle East FZE (Dubai-UAE). Deionized water used in all experiments was prepared in a three-stage Millipore Milli-Q plus 185 purification system and had resistivity of 18.2 mΩ cm.

Process Details. Figure 1a shows a schematic of the process for sc-CO_2 assisted nebulization, a continuous flow process, in which a stream of sc-CO_2 is mixed with an aqueous stream containing the solute of interest and the mixture allowed to expand at atmospheric pressure after passing through a heat exchanger. Upon mixing, the CO_2 dissolves in the aqueous phase at high pressure (CO_2 solubility in water: 2.2 mol % at 40 °C and 100 bar[38]). The aerosol is generated during depressurization in a two-step process:[34] First, the undissolved sc-CO_2 phase expands to gaseous CO_2 and creates a dispersion of aqueous droplets that are supersaturated with CO_2. In the second step, these droplets undergo further breakdown because of a rapid release of the dissolved CO_2 gas, resulting in a fine aerosol with 0.1–3 μm particle size. The dense aerosol is then directed onto heated substrates where rapid effervescence of CO_2 as well as evaporation of the microdroplets takes place and microstructures are generated depending on the time of deposition. The microstructures are further sintered at 300–450 °C to induce decomposition of remaining organic salts and to create nanosized pores within the walls of the microstructures.

In our experiments, the flow rate of sc-CO_2 was adjusted to maintain constant pressure and the aqueous solution was pumped at a constant mass flow rate. A range of experiments was carried out initially to establish the operating space in terms of pressure, temperatures, flow rates, capillary dimensions, and spray tip location. The process was designed to mix two streams, namely, sc-CO_2 and an aqueous solution at constant pressure and temperature in a static mixer. Once mixed, the solution streams were depressurized either through a 50.8 mm long, 1.59 mm inner diameter (ID) stainless steel (S.S.) tubing or a 25.4 mm long, 125 μm diameter stainless steel capillary tube or a sapphire nozzle with 125 μm diameter.

A transport table was installed underneath the spray on which an aluminum heating block was mounted. The heating block could be raised and lowered to adjust the spray distance. Substrate temperature was controlled, by tuning the heat input to the aluminum block. The mounting block had screws at its corners to hold 50.8 mm × 50.8 mm substrates to be coated by the depressurized spray. The translational
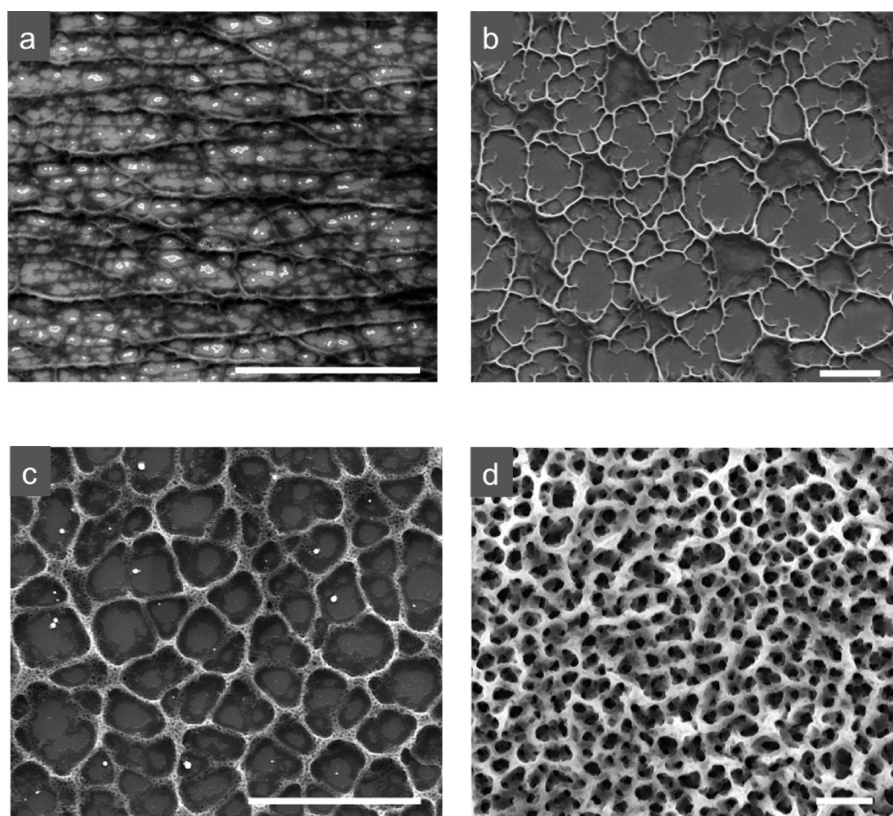
Figure 2. Morphologies of $CaCO_3$ scaffolds obtained by aerosol deposition process: (a, b) nanowires and (c, d) membrane-like scaffolds (each scale bar is 5 μm).

table was capable of moving the substrate under the spray at a given rate (e.g., 12.7 mm·sec^{-1}).

The following general experimental conditions were used. Flow rate of aqueous solution (0.1 wt %) ranged from 1 to 4 g min^{-1}. Sc-CO_2 was used to adjust the pressure in the mixer in the range of 65−130 bar. Mixing chamber temperature was always maintained at 100 °C. Sc-CO_2 line temperature up to the mixing chamber was at 100 °C. We generally used a 50.8 mm × 50.8 mm silicon wafer mounted to the heated aluminum block on the translation table. Experiments were carried out with quartz and sapphire wafers as well. The temperature of the aluminum block was controlled throughout the experiment and at a range of 80−200 °C was used. The tip of the 1.59 mm S.S. tubing was mounted at either 25 mm or 50 mm above the silicon substrate, which was moved back and forth (cycled) at 12.7 mm s^{-1}. The coating time ranged up to 20 min. In all cases, the samples were post-treated at a higher temperature range of 450 °C for at least 3 h.

Characterization. Surface morphology of the thin films was characterized by field-emission scanning electron microscopy (FE-SEM, FEI, The Netherlands) and by atomic force microscopy (AFM, Agilent) in the tapping mode. Height, phase and amplitude images were acquired simultaneously. The cantilevers (Nanosensors , Neuchatel, Switzerland) with frequency of 204−497 kHz and force constant of 10−130 N m^{-1} were used. The set point ration was kept 0.9. Gwyddion free software was used to process acquired images. ImageJ software (http://imagej.nih.gov/ij/) was used for analysis of SEM images.

X-ray measurements were made using a Panalytical Empyrean X-ray diffractometer equipped with a Cu anode X-ray tube. The X-rays were focused using a parallel mirror fitted with 0.02 rad Soller slits and 1/32° divergent slit, on the sample. The sample was aligned for X-ray reflectivity, viz. substrate parallel to the X-ray beam and blocking one-half of the incident intensity. The diffracted X-rays passed through a 0.27° parallel plate collimator and 0.02 rad Soller slits to a proportional detector. The measurements that are presented were made with the same step sizes and times per step.

Optical and Raman microscopy were performed on a WiTec alpha 300 confocal Raman microscope equipped with 50X and 100X objectives. Pinhole diameter of the confocal microscope was kept constant at 100 μm. Raman spectra were acquired using 532 nm laser for excitation (12 mW power) and recorded using a CCD camera maintained at −60 °C. Integration time for acquisition of spectra was kept constant at 3 s. Each spectrum is an average of 10 consecutive scans. Films were rescanned after data acquisition to detect radiation-induced damage. No chemical change in the film composition was detected for exposure time of 30 s at 12 mW power.

Dynamic water contact angle measurements were carried out using a SCA-20 from Data Physics at room temperature. The thickness measurements of calcinated $CaCO_3$ scaffolds were performed on a Dektak XT (Bruker). Height profiles were collected from scratches made on the scaffold. The resulting profiles were analyzed by Vision64 software. The measurements were repeated at least three times.

Application of $CaCO_3$ on Titanium Implants and Preclinical Model Testing. For this purpose, a total of 24 grade II (commercially pure) titanium alloy implants were obtained from a medical device manufacturer (Emfil, Itu, Sao Paulo). These devices were screw shaped and presented 4 mm in diameter and 10 mm in length. Half of the implants had their surfaces coated with $CaCO_3$ through the methodology presented above and the other half remained uncoated. Following coating, the implants were γ radiation sterilized.

The preclinical laboratory in vivo model selected was the sheep ($n =$ 6 animals). The study was approved by the Ethics Committee for Animal Research at the École Nationale Vétérinaire d'Alfort (protocol number 13−011; 14/05/13−3 -Maisons-Alfort, Val-de-Marne, France). The Finnish Dorset crossed-bred sheep (each weighing approximately 150 pounds) were approximately 1.5 years old remained in the facility for 2 weeks prior to the surgical procedures. A total of 24 implants were distributed among 2 experimental groups ($n = 6$ per group and time-point, four per animal. The pelvis access was performed by an antero-posterior incision of 15 cm in length, which was followed by bunt dissection of the fat and muscle layers.
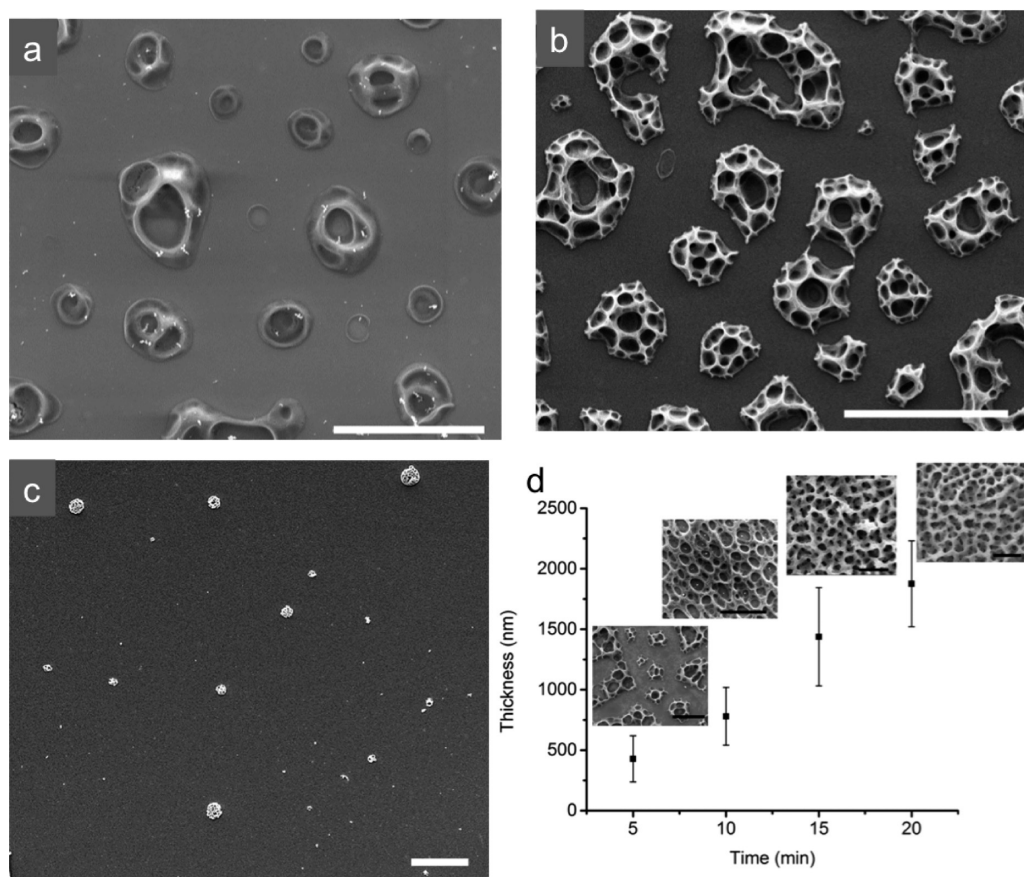
Figure 3. Effect of temperature on the morphology of deposited scaffolds: (a) T = 80 °C, (b) T = 130 °C, and (c) T = 150 °C. d shows the evolution of scaffold thickness and morphology with time for T = 130 °C and P = 120 bar (scale bar in a−c is 10 μm; scale bar in d is 5 μm).

The implants were placed sequentially from proximal to distal at a distance of 2 cm from the first implant's center at the central region of the bone. On each sheep, 2 implants were first placed in one side of the hip, and after 5 weeks, the other side of the hip underwent the same procedure (4 sites per animal). One week later the animals were sacrificed and thus each animal provided samples that remained in vivo for 1 and 6 weeks. All surgeries were conducted under general anesthesia and postoperatory procedures as previously reported.[39]

Following sacrifice, the implants in bone were reduced to blocks and processed for nondecalcified histologic sections. The 30 μm sections were Stevenel's Blue Von Gieson's fuchsin acid stained and referred to histometric measurement of the Bone Area Fraction Occupancy (BAFO) of the region between implant threads performed by an experienced operator by computer software (ImageJ). The statistical evaluation of the effects of time and implant surface on BAFO measures was performed by a Wilcoxon sign rank test. Statistical significance was set at 5% (α = 0.05).

■ RESULTS AND DISCUSSION

Using the methods described in this study, porous films with a dual hierarchy of pore sizes were produced: pores with 1−3 μm diameter, created by pattern formation during the evaporation of solution microdroplets, and smaller pores with ∼50 nm diameter, created in the walls of the bigger pores by a subsequent sintering step. Our method is quite general and can be applied for the formation of films from a wide variety of ceramic materials, such as Co-doped ZnO, CuO, and Ag$_2$O (Figure 1b−d). Fabrication of different morphologies is possible by simply changing the process parameters, as illustrated in Figures 2a−d for the deposition of CaCO$_3$ films under different conditions. CaCO$_3$ is chosen as a model

material because of its important applications in tissue engineering. Depending on the amount of material deposited, we observe different morphologies such as a network of nanowires (Figure 2a, b) or porous scaffolds of different thicknesses (Figure 2c, d). The nanowires formed during initial stages of deposition exhibit significant stick−slip motion of the contact line during evaporation and evolve into thicker walls of the micropores with continued deposition. This behavior is consistent with the observations of evaporating nanofluid droplets by Sefiane et al.[40−43]

Effect of Process Parameters on Microstructure Formation. The main purpose of this paper is to report our invention that leverages the phenomenon of the "coffee-ring" effect to create a scalable process platform to generate meso- and nanoscale structures of a broad class of inorganic materials and a combination of them, from a single source stream. In addition, we have probed the qualitative influence of various process parameters on the deposited microstructures using calcium acetate as a precursor compound. More detailed, quantitative process optimization studies for several compounds will be described in subsequent publications. In the following discussion, we describe our results qualitatively using calcium acetate as a precursor although similar experiments were conducted for other materials as well. We then follow with discussing the results obtained in our in vivo preclinical laboratory model.

The overall process of formation of the microstructures is complex and strongly influenced by the following parameters: the pressure of the CO$_2$ stream, the droplet size as well as the

　　　dx.doi.org/10.1021/am505318d | *ACS Appl. Mater. Interfaces* 2014, 6, 20643−20653

number density of the aerosol, concentration and nature of the solute dissolved, wettability and thermal conductivity of the substrate, temperature of the heated substrate, and the deposition time. First we studied the effect of CO_2 pressure on the aerosol dynamics and the formation of microstructures. Pressure is an important parameter since it affects the solubility of CO_2 in water, the flow dynamics of the aerosols produced, and also the amount of Joule−Thomson cooling that accompanies the expansion. Solubility of CO_2 is directly proportional to the pressure (Henry's law), whereas the flow dynamics is affected by the pressure as well as geometry of expansion. For a given flow geometry, the Joule−Thomson effect limits the operating pressure to a value above which there is significant condensation of dry ice in the flow. We explored the following geometries of expansion: a 125 μm diameter plain orifice (aspect ratio 5), 125 μm diameter capillary tube (length 25.4 mm, aspect ratio 203), and 1.59 mm diameter stainless steel tube (length 50.8 mm, aspect ratio 32). We observed that pressures up to 300 bar could be realized using either the nozzle or the capillary tube however there was significant Joule-Thomson cooling that led to the condensation of dry ice and caused an intermittent flow if sufficient external heating was not provided. The morphologies of microstructures obtained using different flow geometries were largely similar even though the mass flow rates of the aerosols were significantly different. The large diameter stainless steel tubing produced aerosols with higher mass flow rates and required shorter exposure times for the deposition of similar amounts of materials. Unless otherwise specified, experiments were conducted using the 1.59 mm diameter stainless steel tube for expansion. Figure S1 (see the Supporting Information) shows the effect of CO_2 pressure on the morphology of $CaCO_3$ microstructures formed at 80 and 100 bar pressures. The pore size is similar (1−3 μm); however, the pore walls appear to be broader at lower pressure (0.33 ± 0.20 μm at 100 bar vs 1.04 ± 0.13 μm at 80 bar) for the same deposition time. On the basis of the outcomes of different pressure experiments P = 120 bar was chosen as the operating pressure.

Keeping the operating pressure constant, we investigated the effect of surface temperature on the morphology of the microstructures. Films were deposited at different surface temperatures and were examined under FE-SEM after sintering at 300−450 °C. Figure 3a−c shows different patterns of dried droplets depending on substrate temperatures in the range 80−160 °C. When the aerosol droplets were collected at surface temperature of 80 °C (Figure 3a), we observed drying patterns consistent with single droplet drying events as well as coalescence of droplets, either on the surface or in-flight. At elevated temperature of 130 °C, similar deposition patterns were obtained, however, the number of pores formed were larger and the average pore sizes were smaller (Figure 3b). In this temperature range, the morphologies of dried droplets are somewhat similar to that observed for aerosol droplets drying in flight.[44,45] At substrate temperatures above 150 °C (Figure 3c), we observed that only small amount of material was deposited on the surface. Deposition under these conditions yielded nearly spherical particles that were smaller in size and had different pore structures than those deposited at lower temperatures.

Thermal conductivity of the substrate was found to have negligible effect on the porosity of films even though this parameter has been shown to strongly influence the kinetics of droplet evaporation of sessile droplets on heated sub-

strates[46−49] (the thicknesses and thermal conductivities of the substrates used in our experiments are listed in the Supporting Information, Table ST1, for comparison). We observed no difference in the morphologies of the films deposited under same conditions for these three different substrates. The morphologies were also largely similar in experiments performed with and without the application of thermal grease between the substrate and the aluminum heating block to lower the contact thermal resistance.

Mechanism of Microstructure-Formation. The Weber numbers ($We = (\rho V_{im}^2 D_{im})/\gamma$) for aerosol droplets impinging on heated surfaces (3 μm $\leq D_{im} \leq$ 6 μm; 0.5m/s $\leq V_{im} \leq$ 3 m/s) are small enough ($We \leq 1.0$) so that the phenomena of droplet recoil, jetting, splash, breakup, and rebound do not occur during the deposition. The droplets stick to the surface upon impact and evaporation takes place.

The phenomenon of a single microdroplet drying on a heated surface is itself very complex and influenced by several parameters such as the droplet size, thermodynamic properties of the liquid, surface roughness, surface energy, temperature, and thermal properties of the substrate. Experimental and numerical investigations of the heat and mass transfer[44,48−54] during evaporation of sessile droplets has also been thoroughly studied because of ts relevance in industrial applications such as inkjet printing, spray cooling, and spray coating. There is considerable literature on experimental observations and simulations of single microdroplet evaporation;[55−64] however, the evaporation of multiple particles of aerosol has not been studied in detail.

Most of the spray-coating processes are designed to create thin, continuous films without any voids.[30−32] In our process, the aerosol deposition leads to a porous microstructure. Mechanistic understanding of the process of microstructure-formation can be developed through the interpretation of the effects of various process parameters on the final micro-structure. This interpretation is further abetted by the existing literature about experimental observation and computational modeling of evaporation of microdroplets on heated surfaces. Because of the relevance in inkjet printing and heat transfer in spray cooling, the evaporation of heated water droplets with sizes across the range from few mm to 17 μm diameter has been studied in detail. It is generally observed that, across this size range, the initial evaporation rate scales linearly with the contact radius, surface temperature, and substrate thermal conductivity.[48,49,65] Putnam et al. report experimental observation and simulation results for microdroplet evaporation on a variety of surfaces across a temperature range 25−250 °C.[48] On the basis of their investigations of microdroplets with 30−85 μm diameter, the evaporation rate is initially constant for about half lifetime of the droplet, after which stick−slip contact angle dynamics takes place. The droplet lifetimes are on the order of 100 ms and decrease with droplet size. Grigoropoulos et al.[49] report similar experimental observations for water droplets in the size range 17−50 μm diameter with droplet lifetimes around 10 ms at 110 °C. Droplet lifetimes with a similar order of magnitude can be expected for the aerosol droplets in our experiments.

In our process, the evaporation is further complicated due to the fact that the droplets are saturated with CO_2 gas when they strike the surface. Even though there is release of CO_2 during aerosol formation, CO_2 has high solubility in water at room temperature and pressure[38,66] which reduces drastically upon heating. Therefore, bubble formation is highly likely to occur as
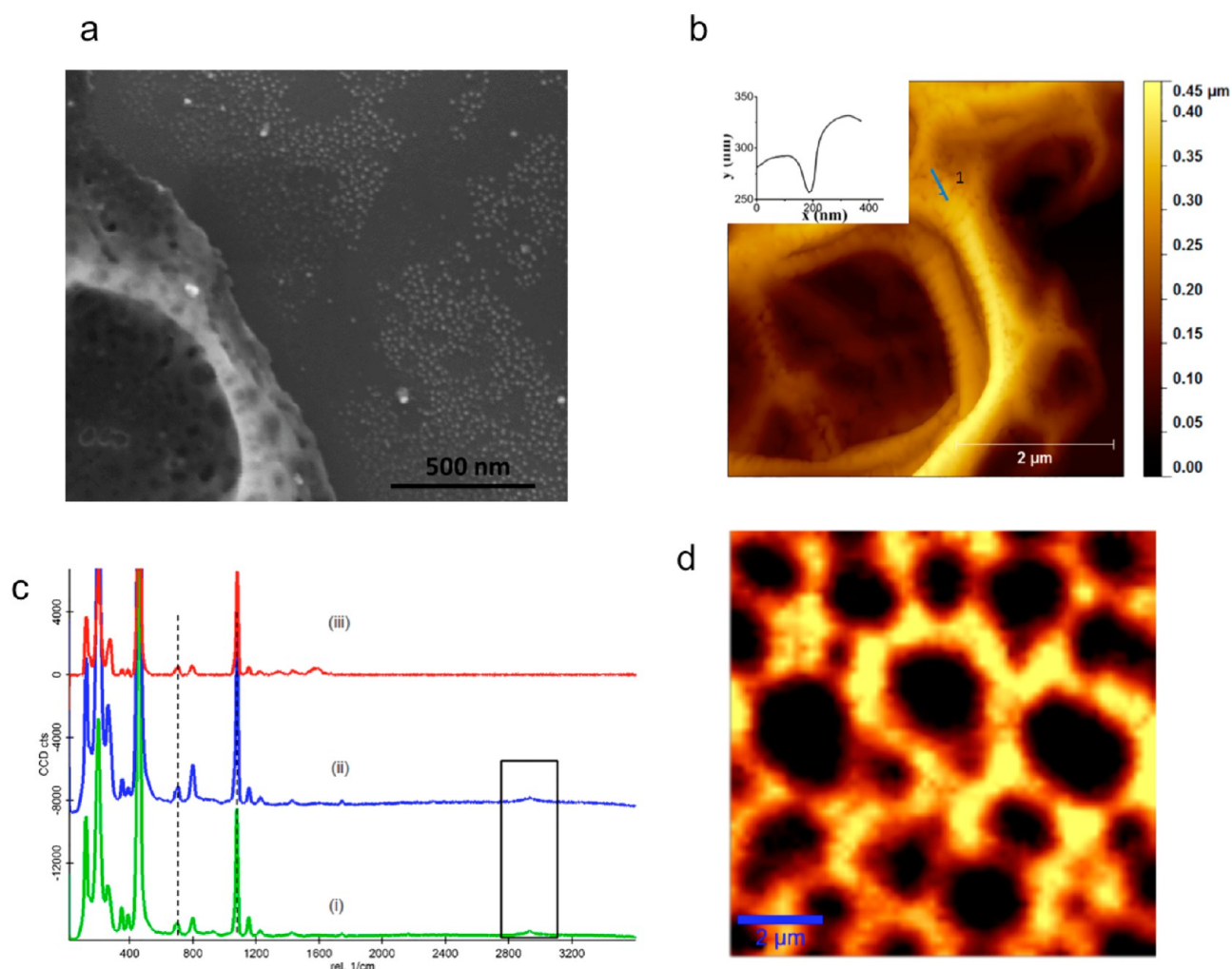
Figure 4. (a, b) Mechanism of nanopore formation after sintering, (c) Micro-Raman analysis of deposited $CaCO_3$ scaffolds: (i) deposited scaffolds without sintering; (ii) deposited scaffolds, nonsintered, washed with water; (iii) scaffolds after sintering and (d) Confocal Raman spectral image of scaffold mapping the intensity of the peak at 1083 cm^{-1} (scale bar 2 μm).

soon as the droplet strikes the surface. Because of the low activation energy, CO_2 effervescence should take place at a much faster rate than the evaporation. On the basis of the solubility data, bubbles of about 1−1.5 μm diameter should form within a 3 μm diameter droplet when heated from 20 to 80 °C. The release of CO_2 results in a decrease in the pH and also affects the ionic equilibrium of the aqueous solution causing precipitation of $CaCO_3$. The formation of bubbles within drying droplets is evident in Figure 3a at temperature below the saturation temperature of water at 1 bar. Dynamics of entrapped vapor bubbles during evaporation of microdroplets on superheated surfaces has been studied by Putnam et al.[58] who observed that the collapse of entrapped bubbles leads to the formation of coffee-rings. In our process, the trapped bubbles can be formed even below the saturation temperature due to the dissolved CO_2 and can significantly enhance the coffee-ring effect (Figure 3a, b).

The observed patterns of nanowires (Figures 1c, 1d, and 2a) are seen for short deposition times of aerosols produced using either the nozzle or the capillary wherein the mass-flow rates are considerably lower than those produced using the 1.59 mm diameter stainless steel tubing. Indeed, similar patterns are also observed for deposition of the aerosols produced using the later geometry of expansion but only in the regions of low droplet

impact probability. Figure S2 in the Supporting Information shows one such shadowed region where the paths of drying droplets could be clearly seen. The droplets appear to be quite mobile and move along the flow of gas leaving behind the elongated coffee-rings. Within short deposition time, the surface should be covered with a mesh of nanowires.

Once the region is entirely covered with nanowires, an additional mechanism needs to be considered. The impacting droplets are expected to get pinned right away due to the increased roughness of the surface in the presence of nanowires. In spite of the short droplet lifetime (∼10 ms), there could be considerable on-surface coalescence as well since the aerosol is dense. This may lead to the patterns observed in Figure 3a, b. Continued deposition takes place preferentially along the periphery of the droplets increasing the breadth and height of the walls of the isolated microstructures. These isolated microstructures finally merge together resulting in the formation of membrane-like patterns shown in Figures 1b and 2c, d, obtained after long-term deposition. We observe that the walls of the microstructures get thicker as the film thickness increases. With continued deposition, although the film thickness grows, the thermal conductivity of the surface drops because of the porous structure and the kinetics of film growth slows down. The thickness growth of $CaCO_3$ scaffolds
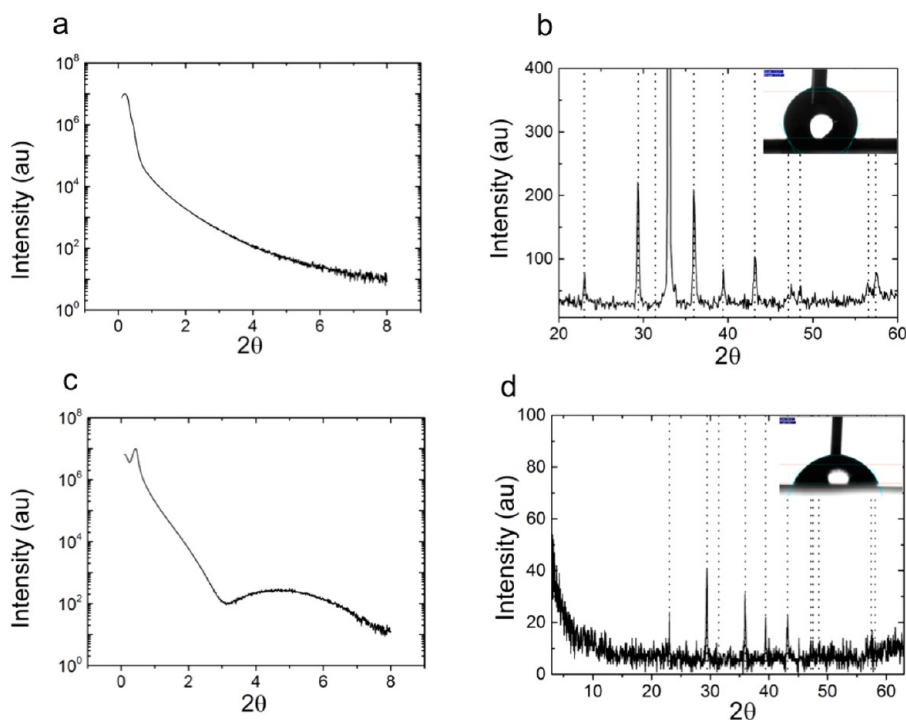
Figure 5. (a, c) XRR and (b, d) XRD patterns of porous CaCO$_3$ scaffolds (a, b) sintered immediately after coatings were prepared and (c, d) coatings were immersed in deionized water at room temperature for 30 min after the substrates were coated with the scaffolds. Insets in b and d show water droplets in contact with the scaffolds. The nanoporous scaffolds in b exhibit a higher, hydrophobic contact angle of 117°. Interestingly, the two-dimensional CaCO$_3$ sheets exhibit a lower, hydrophilic contact angle of 67°.

(measured perpendicular to the substrate) within 20 min deposition time is shown in Figure 3d. During the deposition, the range of micropore size does not change significantly (see Figure S3 in the Supporting Information), even though the scaffold thickness increases gradually from 500 to 2000 nm.

Mechanism for Formation of Nanosized Pores. Figure 4 shows a typical CaCO$_3$ scaffold prepared under optimal process conditions (P = 120 bar, T = 130 °C, t = 20 min) with pore diameter of 1−3 μm. We also observed the presence of a secondary structure of nanosized pores within the CaCO$_3$ scaffolds (Figure 4a). AFM analysis confirmed the pore sizes to be around 50 nm (Figure 4b; distribution of nanopore size is shown in Supporting Information, Figure S4; on the basis of the AFM analysis, nanopore diameter = 50 ± 14 nm). We believe that the nanosized pore formation takes place during the sintering step because of the release of CO$_2$ gas, either trapped or formed via decomposition of residual Ca-(CH$_3$COO)$_2$ precursor. Micro-Raman analysis (Figure 4c, d) indicates that the nonsintered films mostly contain CaCO$_3$ (band at 1083 cm^{-1}, ν_1 symmetric stretch, CO$_3^{2-}$) formed by the precipitation in carbonated water droplets. However, the presence of residual Ca(CH$_3$COO)$_2$ precursor in small quantities is also seen by the band at 2928 cm^{-1} corresponding to C−H stretch, which is not present in the Raman spectrum of sintered films. When the nonsintered films were immersed in a bath of deionized water for 30 min at room temperature, the acetate bands, while slightly diminished in intensity, were still very much present in the water-treated samples. This indicated that the acetate components were buried within and protected by the CaCO$_3$ deposits. During sintering, the release of gaseous products results in the formation of the porous structure. The advancing water contact angles of CaCO$_3$ films also increase

from 67 to 117° upon sintering because of the formation of nanosized pores (Figures 5 b and 5d insets).

Panels a and b in Figure 5 show the low-angle (XRR) and wide-angle (XRD) X-ray scattering results for CaCO$_3$ scaffolds, which were sintered immediately after the coating process was completed. It is interesting to note that although no significant low angle features were observed, XRD confirmed the presence of calcite CaCO$_3$ [ICDD Reference 00−005−0586]. Though calcite is rhombohedral in structure (space group $R\overline{3}c$ (167)) the unit cell is commonly reported with hexagonal unit cell parameters, a = b = 4.989 Å, c = 17.062 Å. Although many of the existing literature studies report domination of {104} texture (29.4° 2θ diffraction peak), the CaCO$_3$ scaffolds reported in our work show evidence of some degree of {110} texture of calcite based on the stronger than expected intensity of the (110) calcite diffraction peak at $2\theta \approx 35°$.

Figure 5c, d show the low-angle (XRR) and wide-angle (XRD) X-ray scattering data for the coating, which was immersed in a bath of deionized water at room temperature for 30 min. These samples were not sintered. The low-angle XRR pattern (Figure 5c) clearly shows a $2q$ peak at 5.3°, indicating a layered thickness of 16.5 Å consistent with a nanostructure. Although the solubility of bulk CaCO$_3$ in deionized water is low the small amount of total CaCO$_3$ in a coated film and the high surface area to surface volume ratio of the nanosheets likely give rise to surface recrystallization resulting in the reduction of surface roughness and the reduction of variance in the thickness of the nanosheets, leading to the observation of the XRR peak in Figure 5c. Interestingly, the wide-angle XRD data (Figure 5d) showed sharp diffraction peaks similar to those observed in Figure 5b, indicating the nanostructure must be well-aligned and ordered resulting in the observed sharp peaks in the wide−angle diffraction pattern of Figure 5d. Using the
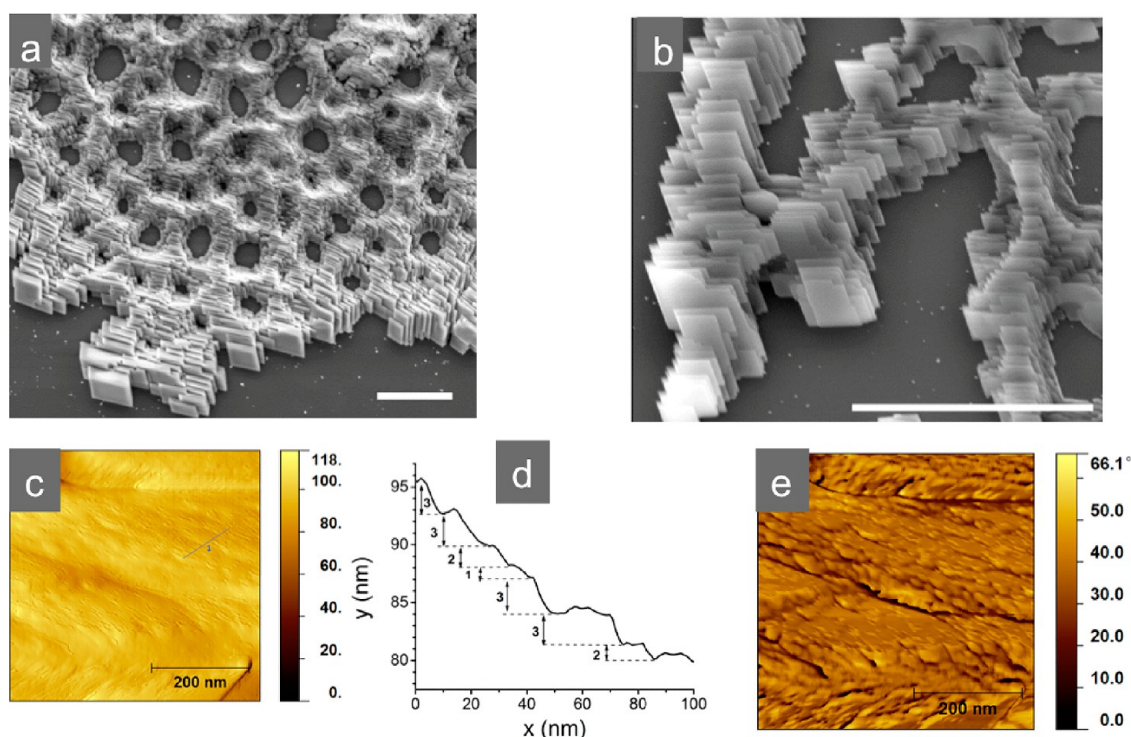
Figure 6. (a, b) SEM, (c−e) AFM images of CaCO₃ scaffolds after 30 min water immersion treatment. Image c represents topography, image d the height profile, and e the phase image. Scale bar on images a and b is 3 μm.
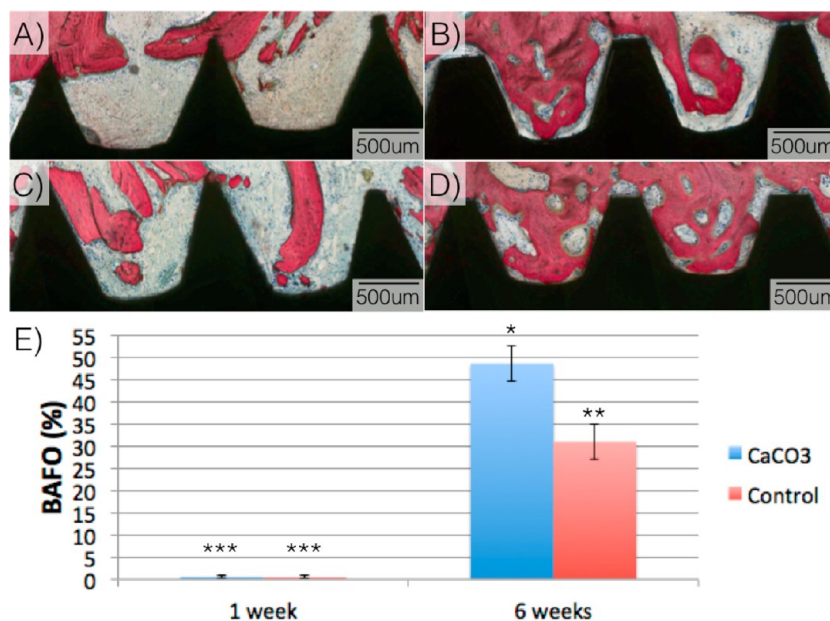

Figure 7. (a−d) Optical micrographs of thin implant in bone slices depicting the different groups at (a, c) 1 week and (b, d) 6 weeks in vivo. Both (a) control and (b) CaCO₃ implants barely presented new bone formation and between implant threads only residual pristine bone was encountered along with osteogenic connective tissue (stained green with blue cells). At 6 weeks, higher amounts of bone was observed between the threads of both groups relative to 1 week, where the (c) control implant presented lower amounts compared to the (d) CaCO₃ implant. (e) Statistical analysis showed that the CaCO₃ implant presented significantly higher bone-area-fraction occupancy (BAFO) compared to the control implant at 6 weeks in vivo. The number of asterisks depict statistically homogeneous groups.

Scherrer technique based on the XRD peak widths,[67] the average crystallite size for the water immersed sample was calculated to be 470 Å, larger than the layer thickness determined from the respective low-angle reflectivity pattern. A similar result is reported for graphene fibers generated from the chemical reduction of graphene oxide.[68] Though graphene is a single layer of graphite and should show broad diffuse wide-angle XRD peaks in a diffraction pattern, XRD data for the resulting stacked sheets of graphene showed a sharp (002) diffraction peak ,indicating that ordered layering of nanosheets resulted in what appeared to be a material with a large crystallite size.

It is also interesting to observe that the water immersion process has led to a radical change in the morphology of the $CaCO_3$ films. While the original scaffold structure remained, it is now entirely made up of stacks of well-aligned $CaCO_3$ sheets (Figures 6a & 6b). AFM characterization (Figures 6c, 6d, and 6e) confirmed the presence of extremely well aligned, stacks of sheets, almost resembling surface growth steps on a single crystal, consistent with the wide-angle XRD data, with thicknesses ranging from 1 to 3 nm, consistent with the low-angle XRD data. All of these data strongly imply that the water immersion of the $CaCO_3$ films apparently triggered an Ostwald ripening process, resulting in the creation of these extremely well aligned stacks of 2-dimensional $CaCO_3$ nanosheets. The data suggest that these are two-dimensional, $CaCO_3$ single crystals, with a nominal thickness of approximately 17 Å, the same as a unit-cell dimension for calcite (c-axis = 17.062 Å). The ability to create single unit cell thick, $CaCO_3$ crystalline sheets, (analogous to graphene, in some sense), appears to be a significant discovery. We expect the materials to possess unique properties (e.g., similar to nacre) and plan to thoroughly investigate their mechanical properties.

Preclinical in Vivo $CaCO_3$ on Titanium Implants. No clinical signs of inflammation were observed immediately following surgery or throughout the course of the experiment. No postoperative complications were detected, and no implant was excluded from the study because of the clinical instability immediately after euthanasia.

Histologic observation presented bone formation in close contact to the implant for all groups at both time-points (Figure 7a–d), demonstrating that both coated and uncoated implant surfaces were biocompatible and osseoconductive. Overall, it was evident that the mount of bone between threads substantially increased from 1 to 6 weeks in vivo for both groups. Although no qualitative differences in bone amount were depictable at 1 week in vivo, the amount of the bone appeared higher at 6 weeks for the $CaCO_3$ group (Figure 7c, d) compared to the uncoated surface. From a quantitative standpoint, a significant increase in bone-area-fraction occupancy (BAFO) was observed from 1 to 6 weeks in vivo ($p < 0.001$), something expected for both groups as early bone healing progresses around both implant groups. The mean bone area fraction occupancy percentage results for both groups and times in vivo are presented in Figure 7e and show that at 1 week no significant differences were observed between groups, a result expected because of the early implantation time in vivo where primarily osteogenic connective tissue formation was observed in proximity with the implant surfaces.[69] At 6 weeks, the $CaCO_3$ group presented significantly higher ($p < 0.02$) BAFO than the uncoated group (Figure 7e), unequivocally demonstrating its higher osseoconductive properties that are know to occur due to various factors that include an intimate relationship with the surface and the host biofluids immediately after implantation, the more biocompatible nature of its structure due to its composition, and bone healing hastening achieved though the release of the bioactive ceramic ionic components in vivo.[70]

CONCLUSION

We report the invention of a versatile process that leverages the coffee-ring effect to create nanowires, and hierarchically porous structures for a wide range of metal oxides, carbonates, and mixed metal oxides. The process is uniquely advantaged by the fact that several precursor materials could be codissolved and precipitated from a single source stream, thereby increasing the chemical uniformity in the final structures. The process as described here utilizes sc-CO_2, and hence provides a sustainable, green process platform. An attractive feature of our process design is that it is intrinsically straightforward to scale-up by assembling arrays of spray nozzle heads to coat on wide-format, roll-to-roll, moving surfaces. The resulting porous films with interesting morphologies can lead to improved performance in applications that require high specific surface area, as demonstrated recently by a dramatic increase in the short-circuit current density of dye-sensitized solar cells based on spray-deposited zinc oxide films.[11]

It is clear that the process platform described here has a high potential to enable fabrication of nanomaterial structures that were not yet possible, in a sustainable and commercially scalable fashion. More importantly, we report the discovery of 2-dimensional, single unit cell thick, crystalline $CaCO_3$ sheets (analogous to graphene), as evidenced by SEM, XRD, and AFM. From a biocompatibility standpoint, we successfully hastened bone formation around titanium implant by incorporating $CaCO_3$ to their surface.

■ ASSOCIATED CONTENT

ⓢ Supporting Information

Thickness and thermal conductivities of the substrates (Table ST1), effect of pressure on the morphology of deposited scaffolds (Figure S1), deposition pattern in a shadowed region with low probability of droplet impact (Figure S2), size distribution of micropores from image analysis of SEM images (Figure S3), and size distribution of nanopores formed by sintering of microporous $CaCO_3$ films at 300−450 °C (Figure S4). This material is available free of charge via the Internet at http://pubs.acs.org.

■ AUTHOR INFORMATION

Corresponding Author

*E-mail: rj31@nyu.edu.

Notes

The authors declare the following competing financial interest(s): We have filed a patent application with the US PTO based on this work..

■ ACKNOWLEDGMENTS

■ REFERENCES

(1) Fratzl, P. Biomimetic Materials Research: What Can We Really Learn from Nature's Structural Materials? *J. R. Soc., Interface* **2007**, *4*, 637−642.

(2) Su, B.-L.; Sanchez, C.; Yang, X.-Y. Insights into Hierarchically Structured Porous Materials: From Nanoscience to Catalysis, Separation, Optics, Energy, and Life Science. In *Hierarchically Structured Porous Materials (From Nanoscience to Catalysis, Separation, Optics, Energy, and Life Science)*; Su, B.-L.; Sanchez, C.; Yang, X.-Y., Eds.; Wiley−VCH: Weinheim, Germany, 2012; pp 3−27.

(3) Zhu, Y.; Morisato, K.; Li, W.; Kanamori, K.; Nakanishi, K. Synthesis of Silver Nanoparticles Confined in Hierarchically Porous Monolithic Silica: A New Function in Aromatic Hydrocarbon Separations. *ACS Appl. Mater. Interfaces* **2013**, *5*, 2118−2125.

(4) Sui, Z.-Y.; Cui, Y.; Zhu, J.-H.; Han, B.-H. Preparation of Three-Dimensional Graphene Oxide-Polyethylenimine Porous Materials as Dye and Gas Adsorbents. *ACS Appl. Mater. Interfaces* **2013**, *5*, 9172−9179.

20651

dx.doi.org/10.1021/am505318d | *ACS Appl. Mater. Interfaces* 2014, 6, 20643−20653

(5) He, J.; Chen, J.; Ren, L.; Wang, Y.; Teng, C.; Hong, M.; Zhao, J.; Jiang, B. Fabrication of Monodisperse Porous Zirconia Microspheres and Their Phosphorylation for Friedel-Crafts Alkylation of Indoles. *ACS Appl. Mater. Interfaces* **2014**, *6*, 2718−2725.

(6) Zhang, J.; Wang, S.; Xu, M.; Wang, Y.; Zhu, B.; Zhang, S.; Huang, W.; Wu, S. Hierarchically Porous ZnO Architectures for Gas Sensor Application. *Cryst. Growth Des.* **2009**, *9*, 3532−3537.

(7) Lü, Y.; Zhan, W.; He, Y.; Wang, Y.; Kong, X.; Kuang, Q.; Xie, Z.; Zheng, L. MOF-Templated Synthesis of Porous Co_3O_4 Concave Nanocubes with High Specific Surface Area and Their Gas Sensing Properties. *ACS Appl. Mater. Interfaces* **2014**, *6*, 4186−4195.

(8) Zhu, G.; Xu, H.; Xiao, Y.; Liu, Y.; Yuan, A.; Shen, X. Facile Fabrication and Enhanced Sensing Properties of Hierarchically Porous CuO Architectures. *ACS Appl. Mater. Interfaces* **2012**, *4*, 744−751.

(9) Wang, X.; Liu, W.; Liu, J.; Wang, F.; Kong, J.; Qiu, S.; He, C.; Luan, L. Synthesis of Nestlike ZnO Hierarchically Porous Structures and Analysis of Their Gas Sensing Properties. *ACS Appl. Mater. Interfaces* **2012**, *4*, 817−825.

(10) Tian, J.; Uchaker, E.; Zhang, Q.; Cao, G. Hierarchically Structured ZnO Nanorods-Nanosheets for Improved Quantum-Dot-Sensitized Solar Cells. *ACS Appl. Mater. Interfaces* **2014**, *6*, 4466−4472.

(11) Sarkar, K.; Braden, E. V.; Pogorzalek, S.; Yu, S.; Roth, S. V.; Müller-Buschbaum, P. Monitoring Structural Dynamics of In Situ Spray-Deposited Zinc Oxide Films for Application in Dye-Sensitized Solar Cells. *ChemSusChem* **2014**, *7*, 2140−2145.

(12) Chen, Y.; Zhang, Y.; Baker, J.; Majumdar, P.; Yang, Z.; Han, M.; Chen, F. Hierarchically Oriented Macroporous Anode-Supported Solid Oxide Fuel Cell with Thin Ceria Electrolyte Film. *ACS Appl. Mater. Interfaces* **2014**, *6*, 5130−5136.

(13) Jeon, J.-W.; Sharma, R.; Meduri, P.; Arey, B. W.; Schaef, H. T.; Lutkenhaus, J. L.; Lemmon, J. P.; Thallapally, P. K.; Nandasiri, M. I.; McGrail, B. P.; et al. In Situ One-Step Synthesis of Hierarchical Nitrogen-Doped Porous Carbon for High-Performance Supercapacitors. *ACS Appl. Mater. Interfaces* **2014**, *6*, 7214−7222.

(14) Zhu, M.; Meng, D.; Wang, C.; Diao, G. Facile Fabrication of Hierarchically Porous CuFe2O4 Nanospheres with Enhanced Capacitance Property. *ACS Appl. Mater. Interfaces* **2013**, *5*, 6030−6037.

(15) Coridan, R. H.; Arpin, K. A.; Brunschwig, B. S.; Braun, P. V.; Lewis, N. S. Photoelectrochemical Behavior of Hierarchically Structured Si/WO3 Core-Shell Tandem Photoanodes. *Nano Lett.* **2014**, *14*, 2310−2317.

(16) Luckarift, H. R.; Sizemore, S. R.; Farrington, K. E.; Roy, J.; Lau, C.; Atanassov, P. B.; Johnson, G. R. Facile Fabrication of Scalable, Hierarchically Structured Polymer/carbon Architectures for Bioelectrodes. *ACS Appl. Mater. Interfaces* **2012**, *4*, 2082−2087.

(17) Chae, W.-S.; Van Gough, D.; Ham, S.-K.; Robinson, D. B.; Braun, P. V. Effect of Ordered Intermediate Porosity on Ion Transport in Hierarchically Nanoporous Electrodes. *ACS Appl. Mater. Interfaces* **2012**, *4*, 3973−3979.

(18) Sohn, H.; Gordin, M. L.; Xu, T.; Chen, S.; Lv, D.; Song, J.; Manivannan, A.; Wang, D. Porous Spherical Carbon/Sulfur Nano-composites by Aerosol-Assisted Synthesis: The Effect of Pore Structure and Morphology on Their Electrochemical Performance as Lithium/sulfur Battery Cathodes. *ACS Appl. Mater. Interfaces* **2014**, *6*, 7596−7606.

(19) Bonfield, W. Designing Porous Scaffolds for Tissue Engineering. *Philos. Trans. R. Soc., A* **2006**, *364*, 227−232.

(20) Liu, Y.; Li, J. P.; Hunziker, E. B.; Groot, K. De Incorporation of Growth Factors into Medical Devices via Biomimetic Coatings. *Philos. Trans. R. Soc., A* **2006**, *364*, 233−248.

(21) Jones, J. R.; Lee, P. D.; Hench, L. L. Hierarchical Porous Materials for Tissue Engineering Hierarchical Porous Materials for Tissue Engineering. *Philos. Trans. R. Soc., A* **2006**, *364*, 263−281.

(22) Hollister, S. J. Porous Scaffold Design for Tissue Engineering. *Nat. Mater.* **2005**, *4*, 518−524.

(23) Sai, H.; Tan, K. W.; Hur, K.; Asenath-Smith, E.; Hovden, R.; Jiang, Y.; Riccio, M.; Muller, D. A.; Elser, V.; Estroff, L. A.; et al. Hierarchical Porous Polymer Scaffolds from Block Copolymers. *Science* **2013**, *341*, 530−534.

(24) Pinto, J.; Dumon, M.; Rodriguez-Perez, M. A.; Garcia, R.; Dietz, C. Block Copolymers Self-Assembly Allows Obtaining Tunable Micro or Nanoporous Membranes or Depth Filters Based on PMMA: Fabrication Method and Nanostructures. *J. Phys. Chem. C* **2014**, *118*, 4656−4663.

(25) Krogman, K. C.; Lowery, J. L.; Zacharia, N. S.; Rutledge, G. C.; Hammond, P. T. Spraying Asymmetry into Functional Membranes Layer-by-Layer. *Nat. Mater.* **2009**, *8*, 512−518.

(26) Deegan, R. D.; Bakajin, O.; Dupont, T. F.; Huber, G.; Nagel, S. R.; Witten, T. A. Contact Line Deposits in an Evaporating Drop. *Phys. Rev. E: Stat. Phys., Plasmas, Fluids, Relat. Interdiscip. Top.* **2000**, *62*, 756−765.

(27) Baldwin, K. A.; Granjard, M.; Willmer, D. I.; Sefiane, K.; John, D. Drying and Deposition of Poly(ethylene Oxide) Droplets Determined by Péclet Number. *Soft Matter* **2011**, *7*, 7819.

(28) Sefiane, K. Patterns from Drying Drops. *Adv. Colloid Interface Sci.* **2014**, *206*, 372−381.

(29) Sefiane, K. On the Formation of Regular Patterns from Drying Droplets and Their Potential Use for Bio-Medical Applications. *J. Bionic Eng.* **2010**, *7*, S82−S93.

(30) Schindler, M.; Ruderer, M. A.; Perlich, J.; Schwartzkopf, M.; Herzog, G.; Heidmann, B.; Bu, A.; Roth, S. V.; Mu, P. In Situ X - Ray Study of the Structural Evolution of Gold Nano-Domains by Spray Deposition on Thin Conductive P3HT Films. *Langmuir* **2013**, *29*, 2490−2497.

(31) Abdellah, A.; Virdi, K. S.; Meier, R.; Döblinger, M.; Müller-buschbaum, P.; Scheu, C.; Lugli, P.; Scarpa, G. Successive Spray Deposition of P3HT/PCBM Organic Photoactive Layers: Material Composition and Device Characteristics. *Adv. Funct. Mater.* **2012**, *22*, 4078−4086.

(32) Herzog, G.; Benecke, G.; Buffet, A.; Heidmann, B.; Perlich, J.; Risch, J. F. H.; Santoro, G.; Schwartzkopf, M.; Yu, S.; Wurth, W.; et al. In Situ Grazing Incidence Small-Angle X-Ray Scattering Investigation of Polystyrene Nanoparticle Spray Deposition onto Silicon. *Langmuir* **2013**, *29*, 11260−11266.

(33) Sievers, R. E.; Huang, E. T. S.; Villa, J. A.; Engling, G.; Brauer, P. R. Micronization of Water-Soluble or Alcohol-Soluble Pharmaceuticals and Model Compounds with a Low- Temperature Bubble Dryer. *J. Supercrit. Fluids* **2003**, *26*, 9−16.

(34) Sievers, R. E.; Karst, U.; Milewski, P. D.; Sellers, S. P.; Miles, B. A.; Schaerfer, J. D.; Stoldt, C. R.; Xu, C. Y. Formation of Aqueous Small Droplet Aerosols Assisted by Supercritical Carbon Dioxide. *Aerosol Sci. Technol.* **1999**, *30*, 3−15.

(35) Sievers, R. E.; Sellers, S. P.; Carpenter, J. F., Supercritical Fluid-Assisted Nebulization and Bubble Drying, US Patent 6630121 B1, Oct 7, 2003.

(36) Sievers, R. E.; Karst, U., Methods and Apparatus for Fine Particle Formation, US Patent 6095134, Aug 1, 2000.

(37) Sievers, R. E.; Karst, U., Dissolving substance to form solution, mixing with fluid which forms gas on rapid depressurization, depressurization, US Patent Number 5639441, Jun 17, 1997.

(38) Wiebe, R.; Gaddy, V. L. The Solubility of Carbon Dioxide in Water at Various Temperatures from 12 to 40°C and at Pressures to 500 Atmospheres. Critical Phenomena*. *J. Am. Chem. Soc.* **1940**, *62*, 815−817.

(39) Jimbo, R.; Tovar, N.; Anchieta, R. B.; Machado, L. S.; Marin, C.; Teixeira, H. S.; Coelho, P. G. The Combined Effects of Undersized Drilling and Implant Macrogeometry on Bone Healing around Dental Implants: An Experimental Study. *Int. J. Oral Maxillofac. Surg.* **2014**, *43*, 1269−1275.

(40) Orejon, D.; Sefiane, K.; Shanahan, M. E. R. Stick-Slip of Evaporating Droplets: Substrate Hydrophobicity and Nanoparticle Concentration. *Langmuir* **2011**, *27*, 12834−12843.

(41) Askounis, A.; Orejon, D.; Koutsos, V.; Sefiane, K.; Shanahan, M. E. R. Nanoparticle Deposits near the Contact Line of Pinned Volatile Droplets: Size and Shape Revealed by Atomic Force Microscopy. *Soft Matter* **2011**, *7*, 4152.

(42) Askounis, A.; Sefiane, K.; Koutsos, V.; Shanahan, M. E. R. Structural Transitions in a Ring Stain Created at the Contact Line of Evaporating Nanosuspension Sessile Drops. *Phys. Rev. E: Stat. Phys., Plasmas, Fluids, Relat. Interdiscip. Top.* **2013**, *87*, 012301.

(43) Askounis, A.; Sefiane, K.; Koutsos, V.; Shanahan, M. E. R. The Effect of Evaporation Kinetics on Nanoparticle Structuring within Contact Line Deposits of Volatile Drops. *Colloids Surf., A* **2014**, *441*, 855−866.

(44) Koch, J.; Flamigni, L.; Gschwind, S.; Allner, S.; Longerich, H.; Günther, D. Accelerated Evaporation of Microdroplets at Ambient Conditions for the on-Line Analysis of Nanoparticles by Inductively-Coupled Plasma Mass Spectrometry. *J. Anal. At. Spectrom.* **2013**, *28*, 1707.

(45) Yu, Y.; Chen, C.-H.; Shi, Y. A Tin-Based Amorphous Oxide Composite with a Porous, Spherical, Multideck-Cage Morphology as a Highly Reversible Anode Material for Lithium-Ion Batteries. *Adv. Mater.* **2007**, *19*, 993−997.

(46) Dunn, G. J.; Wilson, S. K.; Duffy, B. R.; David, S.; Sefiane, K. The Effect of the Thermal Conductivity of the Substrate on Droplet Evaporation. In *Progress in Industrial Mathematics at ECMI 2006*; Bonilla, L. L.; Moscoso, M.; Platero, G.; Vega, J. M., Eds.; Springer: Berlin Heidelberg, 2008; pp 779−783.

(47) Dunn, G. J.; Wilson, S. K.; Duffy, B. R.; David, S.; Sefiane, K. A Mathematical Model for the Evaporation of a Thin Sessile Liquid Droplet: Comparison between Experiment and Theory. *Colloids Surf., A* **2008**, *323*, 50−55.

(48) Putnam, S. A.; Briones, A. M.; Byrd, L. W.; Ervin, J. S.; Hanchak, M. S.; White, A.; Jones, J. G. Microdroplet Evaporation on Superheated Surfaces. *Int. J. Heat Mass Transfer* **2012**, *55*, 5793−5807.

(49) Lim, T.; Jeong, J.; Chung, J.; Chung, J. T. Evaporation of Inkjet Printed Pico-Liter Droplet on Heated Substrates with Different Thermal Conductivity. *J. Mech. Sci. Technol.* **2009**, *23*, 1788−1794.

(50) Bhardwaj, R.; Longtin, J. P.; Attinger, D. A Numerical Investigation on the Influence of Liquid Properties and Interfacial Heat Transfer during Microdroplet Deposition onto a Glass Substrate. *Int. J. Heat Mass Transfer* **2007**, *50*, 2912−2923.

(51) Duursma, G.; Sefiane, K.; Kennedy, A. Experimental Studies of Nanofluid Droplets in Spray Cooling. *Heat Transfer Eng.* **2009**, *30*, 1108−1120.

(52) Semenov, S.; Starov, V. M.; Velarde, M. G.; Rubio, R. G. Droplets Evaporation: Problems and Solutions. *Eur. Phys. J.: Spec. Top.* **2011**, *197*, 265−278.

(53) Semenov, S.; Starov, V. M.; Rubio, R. G.; Agogo, H.; Velarde, M. G. Evaporation of Sessile Water Droplets: Universal Behaviour in Presence of Contact Angle Hysteresis. *Colloids Surf., A* **2011**, *391*, 135−144.

(54) Semenov, S.; Starov, V. M.; Rubio, R. G.; Velarde, M. G. Computer Simulations of Evaporation of Pinned Sessile Droplets: Influence of Kinetic Effects. *Langmuir* **2012**, *28*, 15203−15211.

(55) Briones, A. M.; Ervin, J. S.; Putnam, S. A.; Byrd, L. W.; Jones, J. G. A Novel Kinetically-Controlled de-Pinning Model for Evaporating Water Microdroplets. *Int. Commun. Heat Mass Transfer* **2012**, *39*, 1311−1319.

(56) Briones, A. M.; Ervin, J. S.; Putnam, S. A.; Byrd, L. W.; Gschwender, L. Micrometer-Sized Water Droplet Impingement Dynamics and Evaporation on a Flat Dry Surface. *Langmuir* **2010**, *26*, 13272−13286.

(57) Hanchak, M. S.; Briones, A. M.; Ervin, J. S.; Byrd, L. W. One-Dimensional Models of Nanoliter Droplet Evaporation from a Hot Surface in the Transition Regime. *Int. J. Heat Mass Transfer* **2013**, *57*, 473−483.

(58) Putnam, S. A.; Byrd, L. W.; Briones, A. M.; Hanchak, M. S.; Ervin, J. S.; Jones, J. G. Role of Entrapped Vapor Bubbles during Microdroplet Evaporation Role of Entrapped Vapor Bubbles during Microdroplet Evaporation. *Appl. Phys. Lett.* **2013**, *071602*, 2010−2014.

(59) Putnam, S. A.; Briones, A. M.; Ervin, J. S.; Hanchak, M. S.; Byrd, L. W.; Jones, J. G. Interfacial Heat Transfer during Microdroplet Evaporation on a Laser Heated Surface. *Int. J. Heat Mass Transfer* **2012**, *55*, 6307−6320.

(60) Pan, Z.; Dash, S.; Weibel, J. A.; Garimella, S. V. Assessment of Water Droplet Evaporation Mechanisms on Hydrophobic and Superhydrophobic Substrates. *Langmuir* **2013**, *29*, 15831−15841.

(61) Semenov, S.; Starov, V. M.; Rubio, R. G. Evaporation of Pinned Sessile Microdroplets of Water on a Highly Heat-Conductive Substrate: Computer Simulations. *Eur. Phys. J.: Spec. Top.* **2013**, *219*, 143−154.

(62) Das, S.; Waghmare, P. R.; Fan, M.; Gunda, N. S. K.; Roy, S. S.; Mitra, S. K. Dynamics of Liquid Droplets in an Evaporating Drop: Liquid Droplet "Coffee Stain" Effect. *RSC Adv.* **2012**, *2*, 8390.

(63) Sobac, B.; Brutin, D. Thermal Effects of the Substrate on Water Droplet Evaporation. *Phys. Rev. E: Stat. Phys., Plasmas, Fluids, Relat. Interdiscip. Top.* **2012**, *86*, 021602.

(64) Xu, W.; Leeladhar, R.; Kang, Y. T.; Choi, C.-H. Evaporation Kinetics of Sessile Water Droplets on Micropillared Superhydrophobic Surfaces. *Langmuir* **2013**, *29*, 6032−6041.

(65) Dunn, G. J.; Wilson, S. K.; Duffy, B. R.; Sefiane, K. The Strong Influence of Substrate Conductivity on Droplet Evaporation. *J. Fluid Mech.* **2009**, *623*, 329−351.

(66) Reid, R. C.; Prausnitz, J. M.; Poling, B. E. The Properties of Gases & Liquids. In *The Properties of Gases & Liquids*; McGraw-Hill, Boston., 1987.

(67) Cullity, B. D. *Elements of X-Ray Diffraction*; Addison-Wesley, Reading, MA, 1978.

(68) Xu, C.; Gao, C. Graphene Chiral Liquid Crystals and Macroscopic Assembled Fibres. *Nat. Commun.* **2011**, *2*, 1−9.

(69) Coelho, P. G.; Jimbo, R. Osseointegration of Metallic Devices: Current Trends Based on Implant Hardware Design. *Arch. Biochem. Biophys.* **2014**, *561C*, 99−108.

(70) Coelho, P. G.; Granjeiro, J. M.; Romanos, G. E.; Suzuki, M.; Silva, N. R.; Cardaropoli, G.; Thompson, V. P.; Lemons, J. E. Basic Research Methods and Current Trends of Dental Implant Surfaces. *J. Biomed. Mater. Res. B Appl. Biomater.* **2009**, *88*, 579−596.